Chapter 8
Powder Forging of Presintered TRIP-Matrix Composites

Markus Kirschner, Sergey Guk, Rudolf Kawalla and Ulrich Prahl

Abstract This chapter addresses bulk forming processes-especially powder forging-used to produce complex shaped components from presintered TRIP-matrix composites. Based on experimentally determined material and process parameters (e.g., shrinkage, Poisson's ratio, elastic modulus, oxidation behavior), extended process maps for compressible materials were presented. Subsequently, a characterization of the material flow as a function of the material conditions was reproduced via the visioplastic method and metallographic analysis, and then connections were drawn between the results and the extended process maps. The knowledge gained was used to develop a powder forging tool for a Gleeble HDS-V40, which was used to conduct model tests aiming to improve the component properties. The tool was equipped with compensating gaps to provide better compaction to the components. To find the optimal compaction for the solid material, different variants of compensating gaps were investigated. The components obtained through this approach were examined on the basis of their mechanical properties and microstructures. Furthermore, the deformation of graded components was analyzed in this study. In addition to the formation of a damage-tolerant interface and the shear strength of the different layers, special attention was paid to process-relevant parameters, such as the maximum deformation degree, the tool and specimen temperature and the pressure holding time.

M. Kirschner (✉) · S. Guk · R. Kawalla · U. Prahl
Institute for Metal Forming, Technische Universität Bergakademie Freiberg, Freiberg, Germany
e-mail: markus.kirschner@imf.tu-freiberg.de

S. Guk
e-mail: sergey.guk@imf.tu-freiberg.de

R. Kawalla
e-mail: rudolf.kawalla@imf.tu-freiberg.de

U. Prahl
e-mail: ulrich.prahl@imf.tu-freiberg.de

H. Biermann and C. G. Aneziris (eds.), *Austenitic TRIP/TWIP Steels and Steel-Zirconia Composites*, Springer Series in Materials Science 298,
https://doi.org/10.1007/978-3-030-42603-3_8

8.1 Introduction

The integration of various properties and functions in a component or in an assembly is constantly increasing to shorten product manufacturing times and enhance resource conservation. The required high functionality of materials often leads to chemical-physical requirements that cannot be met by a single material. In some cases, the use of high-performance materials can lead to compromises. Moreover, the range of properties of these innovative high-performance materials is often insufficient to cover all requirements, which is why composite materials are used to provide a combination of the desired properties.

Powder forging is a combination of sintering and precision forging technology that blends the advantages of sintering technology in terms of component design possibilities, good material utilization and narrow tolerances with the high strength of forged components [1–3]. Powder forging is used to turn pressed and sintered semifinished products into solid components with outstanding material properties for use in all types of applications [4, 5].

Therefore, the main task of powder forging is to achieve full density [6]. Based on the material flow that occurs, two process variants of powder forging exist [3, 7, 8, 9].

– "Hot repressing": Hot compression without significant material flow, which corresponds to uniaxial compression.
– "Upsetting" (also referred to as "flow forging" or "powder forging"): Hot forming process with significant material flow, wherein a preform with a simple shape is formed into a finished part with a more complicated shape.

The special advantage of powder forging over other compacting processes, such as hot isostatic pressing, lies in the combination of forging technology with the advantages of powder metallurgy. Here, the recrystallization to a finer grain structure and the texture, which is introduced into the component during the forging process, are decisive advantages over other processes. In addition, specimens with complex geometries that exhibit excellent mechanical properties can be produced in large quantities without or with very little further mechanical treatment.

Therefore, powder-forged components are used especially for high dynamic and vibration loads [10–12]. This approach can also produce graded components, which means that components can be manufactured with an inexpensive base material by using a second wear-resistant material for the highly stressed regions [1, 2, 13].

However, this capability is of little use in industry, as the final density of reinforced components and the distribution of the reinforcement phase after powder forging are difficult to control [14, 15]. Due to material flow and the forming process, reordering processes occur in the component that cannot yet be precisely defined. In addition, an additional phase, especially if it is a composite material of two different material classes, represents a barrier to compaction in a component during powder forging; thus, achieving a compact material becomes more difficult [16–18].

This work focuses on the development of basic principles for the production of compact components with different property profiles from a transformation-induced

plasticity (TRIP)-matrix composite. The main process used is powder forging in temperature ranges from 700 to 1100 °C, which follows the sintering process. The test specimens have a residual porosity and the forming process in the final stage is characterized as uniaxial deformation with and without lateral material flow. For this purpose, model compression tests are carried out on the forged specimens in a closed die in order to make a detailed statement on the rearrangement processes of ZrO_2 particles due to friction with contact surfaces, in which the local material flow during compaction is analyzed as a function of the geometry of the forming zone. The challenge here is to investigate the compaction process and the material flow during powder forging of homogeneously reinforced and graded materials. A further challenge is investigating the ability to generate a force-transmitting flat phase boundary via powder forging in the previously designed tool. The technological goal is to produce axially graded components during forming while retaining the graded structure when the material flow begins.

8.2 Materials and Methods

The investigated material is a composition of gas-atomized steel powder, which was austenitic in structure ($d_{10} = 12.4$ µm, $d_{50} = 25.9$ µm and $d_{90} = 46.6$ µm), and Mg-PSZ ceramic powder ($d_{10} = 0.2$ µm, $d_{50} = 4.3$ µm and $d_{90} = 30$ µm). The chemical compositions of both the metastable high alloyed TRIP steel (indicated as X3CrMnNi16-7-6) and the ZrO_2 ceramic are given in Table 8.1. The ceramic particle content was set to 0 vol% (0Z), 5 vol% (5Z), 10 vol% (10Z), 15 vol% (15Z), 20 vol% (20Z) and a graded layer structure. The structures of these five contents are shown in Fig. 8.1.

A binder (1.0 wt% Optapix PAF 35, Zschimmer & Schwarz, Burgstädt, Germany) is used to achieve a more homogeneous density distribution in powder pressing. This binder is added to the powder mixture of ZrO_2 and TRIP steel before powder pressing.

The powder pressing took place at room temperature in a one-sided coaxial press with a pressing force of 200–600 kN depending on the desired residual porosity; the specimens used in this process had a diameter of 10 mm and a height of 10 mm. The individual layers of the graded particle distribution have a height of 2 mm and are stacked individually, precompressed with a low force, and then pressed as a complete component. The subsequent debinding and sintering of the specimens after pressing took place in a furnace (Carbo-Lite/Gero HTK 8 MO/16-1). The debinding was completed before the actual sintering process started. This process took place at a heating rate of 300 K/h and a holding time of 1 h at 1100 °C, followed by a cooling rate of 600 K/h under vacuum (10^{-6} mbar) until reaching room temperature.

For the tests, cylindrical specimens with a height of 10 mm and a diameter of 10 mm were produced. Forming was carried out in a Gleeble HDS-V40 rolling simulator from DSI Europe GmbH (path-controlled) at appropriate temperatures, press forces and deformation degrees. For the desired compression of the specimens, the following three silicon nitride dies, shown in Fig. 8.2, with corresponding tungsten

Table 8.1 Nominal chemical compositions of the TRIP steel powder and Mg-PSZ powder

TRIP steel	Fe	C	Cr	Ni	Mn	Si	N	Al	S	Mo	Ti
[wt%]	bal.	0.03	16.3	6.6	7.2	1.0	0.09	0.04	<0.01	<0.01	<0.01

MgO-PSZ	ZrO_2	HfO_2	MgO	SiO_2	Al_2O_3	CaO	TiO_2	Y_2O_3
[wt%]	bal.	1.85	3.25	0.1	1.58	0.06	0.13	0.13

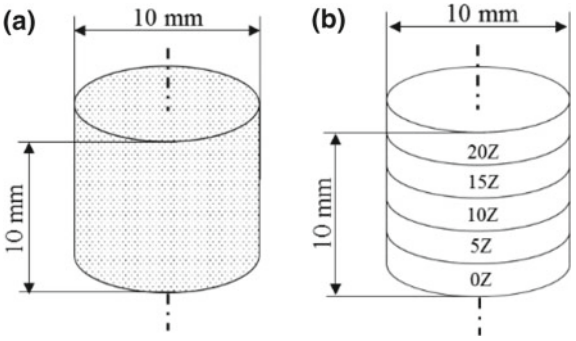

Fig. 8.1 Investigated specimens with **a** homogeneous particle distribution and **b** graded particle distribution

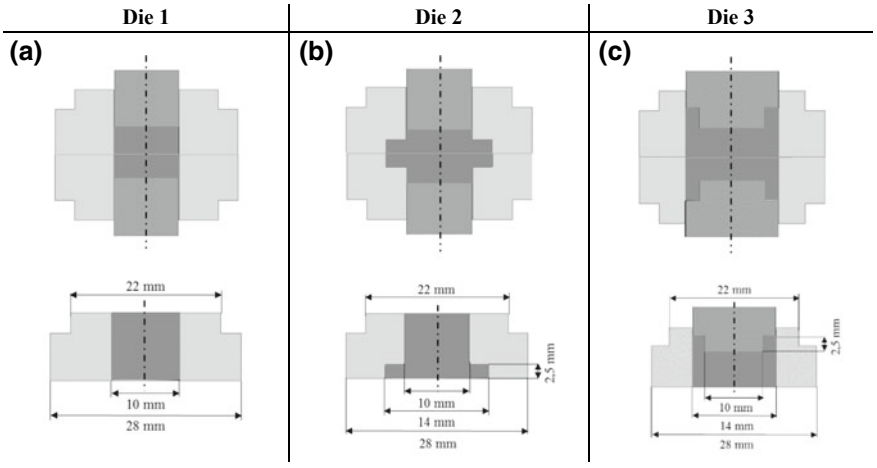

Fig. 8.2 Different die shapes for the investigation of the material flow: **a** Die 1: without a compensating gap; **b** Die 2: with lateral compensating gaps; and **c** Die 3: with upward compensating gaps

carbide punches were available for forming, in which the specimen was conductively heated prior to forming.

Boron nitride was used as a lubricant to reduce friction between the die and the material because carburization may occur during powder forging due to the high temperatures. To avoid this phenomenon, graphite was not used as a lubricant.

The density was determined by means of a hydrostatic balance at room temperature. For this purpose, the specimens were placed in distilled water in a water bath under vacuum for four hours. A magnetic stirrer at the bottom of the water tank prevented the formation of bubbles and kept the water moving. The mass was then determined in distilled water and in air by hydrostatic weighing.

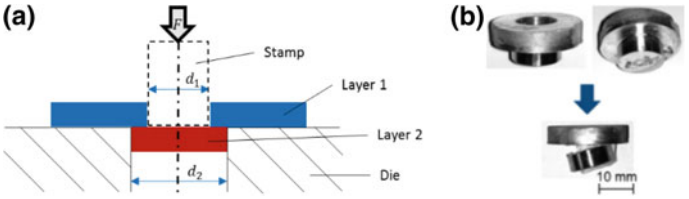

Fig. 8.3 Illustration of the **a** adhesion test and **b** the specimens before and after each test

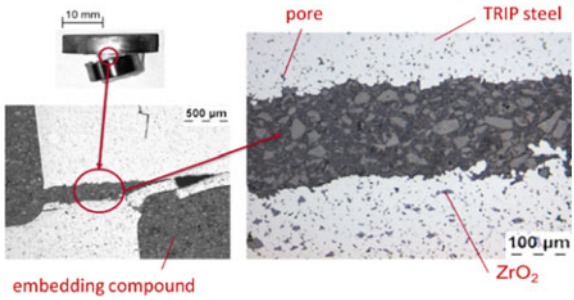

Fig. 8.4 Cross-section through the failure point in an adhesion test specimen

During the adhesion test, the two layers of the graded layer structure of the specimens were generated and the adhesion of the two layers was measured, as shown in Fig. 8.3. The pull-off forces of the individual composite layers were tested in accordance with DIN EN ISO 4624 in an AG-100 testing machine (Hegewald & Peschke, Siebenlehen, Germany). To check whether the phase boundary of the individual layers was also tested, a cross-section was made through the failure point. The results show that the crack did run exactly as desired through the phase boundary of the two structures, as shown in Fig. 8.4.

8.3 Results

To realize this production path, the process-dependent parameters were first examined to limit the process window for the model tests. The focus was on the shrinkage, the density-dependent Poisson's ratio, the density-dependent elastic modulus and the oxidation behavior of the material and on the creation of process maps. Subsequently, model tests were carried out with particular attention to the maximum possible compaction as a function of shear strain, elongation and temperature and to the phase boundary connection between ceramic and steel, which will enable the production of a compact material with complete particle bonding in the matrix. The mechanical properties were then determined from these specimens. Finally, the graded layer structures were investigated following the same approach, and the material properties of the graded layer structures were compared to those of the homogeneous material.

In the following sections, the results of the individual investigations are presented. Note that the analysis takes place in the Cartesian coordinate system and with the different ZrO_2 contents being represented as percentages.

8.3.1 Determination of Material- and Process-Dependent Parameters

Various process parameters were analyzed and evaluated to determine the optimum forging conditions. These parameters include the shrinkage, the density-dependent Poisson's ratio, the elastic modulus/density relationship, and the oxidation behavior of the specimens and process maps. The shrinkage of the components was investigated to calculate the dimensions of the components after sintering and forging, which was necessary for the calculation of the dimensions of the final part and the die dimensions. To consider the density-dependent Poisson's ratio, it is necessary to know the ratio of the horizontal to vertical material load direction when the pore density falls below 10%. The relationship between the density and the elastic modulus was used to determine the start of deformation or plastic flow under external loads. The oxidation behavior was analyzed to investigate the time of transfer between the furnace and the die. Process maps were used to calculate the process window of the different composite states.

8.3.2 Determination of Shrinkage

For the investigation of the specimens after sintering, the shrinkage behavior of the individual ZrO_2 contents was measured with a caliper; the results are shown in Fig. 8.5. The density of the specimens after sintering was 7.1 $\frac{g}{cm^3}$.

The results show that the shrinkage percentage of the sintered specimens reduces considerably with increasing ZrO_2 content. The smallest value of 0.4% can be seen with 20Z, whereas the highest value is 2.2% with 0Z. The specimens with an increasing ZrO_2 content show a decrease in shrinkage. The graded specimen with the value

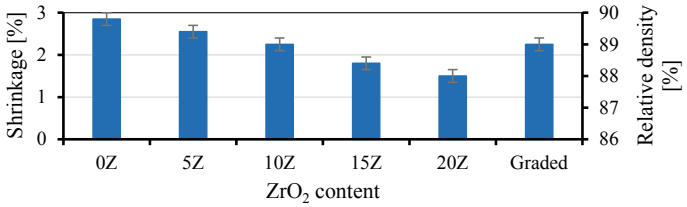

Fig. 8.5 Determination of shrinkage after sintering and powder forging

of 0.7% lies between the specimen with 20Z and the specimen with 15Z. The results also show that there is a considerable difference in shrinkage between the specimen with 0Z and the specimen with 20Z. This difference is important because the shrinkage of the TRIP steel is 2.2%, whereas the shrinkage of ZrO_2 is approximately 0% because the material does not sinter together and is only present as particles in the matrix. Therefore, the shrinkage values of the specimens with a ZrO_2 content are between the shrinkage values of the pure materials. This finding also shows that with increasing ZrO_2 content, the shrinkage of the specimens moves from that of the TRIP steel to that of the ZrO_2 in this particular case.

If these data are compared with shrinkage data from other metal matrix composites (MMCs), it is noticeable that the shrinkage of the TRIP-matrix composite is greater the shrinkage data of other MMCs. For copper matrix composites with a SiC reinforcement phase, the shrinkage is 0.3% [19, 20]. However, note that these specimens had a reinforcement phase content of 70%. A shrinkage of 0.75% was observed in aluminum MMCs, wherein the reinforcement phase was only 0.5% [21, 22]. Thus, the TRIP-matrix composites exhibit greater shrinkage than other particle-reinforced MMCs. However, compared to pure iron steel specimens without particle reinforcement, the specimens in this study exhibit significantly less shrinkage. The high shrinkage in this previous study occurred because a shrinkage of 2.5–3% can be observed in iron powder [23].

Observations show that, similar to the homogenous specimens, the graded specimens exhibit isotropic shrinkage.

The reduction in shrinkage with increasing particle content in the specimens can be explained by the particles themselves. Due to the number of particles in the sintered specimens, there is no specimen shrinkage during sintering because only the matrix material is sintered. The ceramic particles are simply present in the matrix without interacting with the matrix or with each other. The more matrix there is in a specimen, the more the specimen can shrink during sintering. Conversely, this phenomenon means that the more reinforcing particles there are in the matrix (i.e., more of the matrix is replaced), the less the specimen can shrink, as the ceramic particles prevent this shrinkage. This phenomenon can be seen in Fig. 8.5, as the shrinkage of the specimens decreases with increasing ZrO_2 content. The linear expansion coefficient of the matrix is $18.3 \times 10^{-6}\ K^{-1}$, whereas that of ZrO_2 particle is $10.5 \times 10^{-6}\ K^{-1}$.

With regard to shrinkage behavior, there are different approaches that describe the so-called shrinkage parameter. In Fig. 8.6, different shrinkage models are compared to the measured shrinkage of the TRIP-matrix composites. This figure clearly shows that the model according to Coble [24] comes closest to the shrinkage of the TRIP-matrix composite. The value from the Skorokhod model [25] after 60 min of sintering time comes close to the value of the composite, even if the value is an overestimation, whereas the Tikkanen Mäkipirtti model [26] does not show any similarity with the measured value. Note that in the Coble model, the porosity at a certain time works in conjunction with various other material constants, whereas the Skorokhod model and the Tikkanen Mäkipirtti model try to solve the problem via density differences and sample volume differences, respectively.

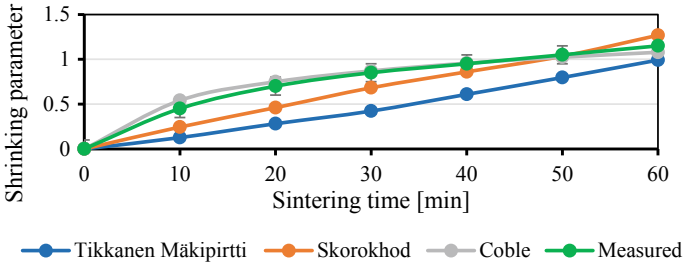

Fig. 8.6 A comparison of different shrinkage models with the measured parameters under the following conditions: 5% ZrO_2 and a residual porosity of 10%

However, in all equations there is no approach for a second material in the equation, which strongly influences the shrinkage parameter due to a different shrinkage. Therefore, the following equation was established on this basis for composite materials:

$$v_s = (-0.13Z + 0.15) \cdot \sqrt{t} \tag{8.1}$$

where Z is the volume content of the second material and t is the sintering time. The equation used here is similar to the equation according to Coble because both equations are based on the specimen porosity and the sintering time. However, this equation further discusses the properties of composites, since the amount of the second phase in the matrix is also taken into account. Thus, a coefficient of determination of 0.98 can be achieved.

8.3.3 Poisson's Ratio as a Function of Density

The Poisson's ratio was determined by compression tests, which were carried out on a Bähr MDS 830 testing system. The Poisson's ratio was determined in accordance with the literature [27]. The specimen was lubricated with boron nitride, and the strain was 0.5 at room temperature.

Figure 8.7 shows that the Poisson's ratio decreases with increasing residual porosity. This finding can also be found in the literature [27]. The reason for this phenomenon is the compression of the material during the compression test with increased residual porosity. The results also show that apart from some fluctuations in the results within the fault tolerance, there are no deviations from the theoretically determined Poisson's ratio. The minor deviations are due to measurement uncertainties.

When considering the dependence of the Poisson's ratio on the density, it is noticeable that the Poisson's ratio increases with increasing density, as shown in Fig. 8.8. This trend corresponds to the general state of the art [27–29]. Furthermore,

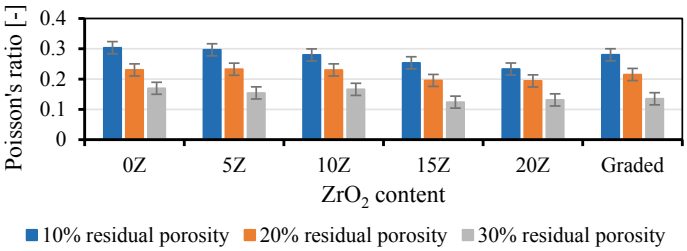

Fig. 8.7 Change in Poisson's ratio under different residual porosities

Fig. 8.8 Dependence of Poisson's ratio on density

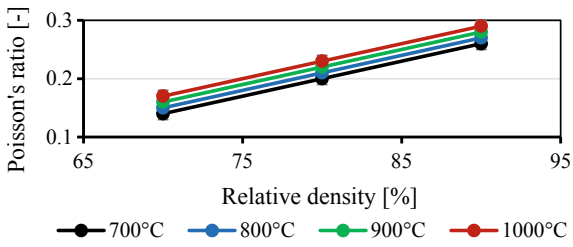

the results show that with increasing density, the Poisson's ratio changes slightly. This trend can be described using the following equation:

$$\vartheta_\rho = (0.6 \cdot \rho_0) + T \cdot 10^{-4} - a \tag{8.2}$$

where ρ_0 is the relative density, T is the working temperature in [°C] and a is a material constant. In this case, a is approximated to a value of 0.35. The equation is an extension equation according to Kuhn and Downey [30]. The equation was extended by the temperature term and a material constant. Nevertheless, the relative density plays a more decisive role in the equation than the temperature. This equation has a determination coefficient of 0.99 with the empirically determined data.

This phenomenon mainly occurs due to the relationship between the elastic modulus, shear modulus and the Poisson's ratio. Due to the heating of the material, the elastic modulus and shear modulus are reduced. As the shear modulus is doubled in the Poisson's ratio formula, the Poisson's ratio increases at higher temperatures.

For upsetting, the ratio of the material flow perpendicular to the pressing direction to that in the pressing direction can be described with a density-dependent Poisson's ratio [8, 30, 31, 32], as shown in Fig. 8.9 for the material here. The figure clearly shows that with increasing ZrO_2 content the density-dependent Poisson's ratio decreases. This phenomenon means that with increasing ZrO_2 content, the ratio of material flow perpendicular to the pressing direction to that in the pressing direction decreases. Moreover, this behavior can be explained by the ZrO_2 particles, which oppose the material flow. For this reason, the ratio of material flow in the pressing direction to that in the pressing direction also decreases.

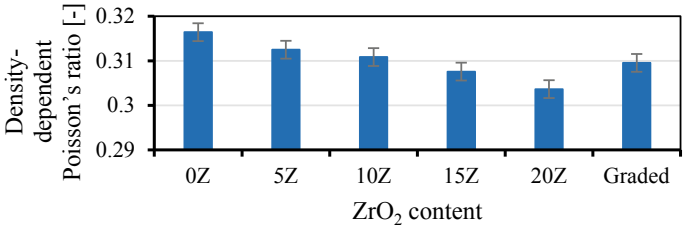

Fig. 8.9 Density-dependent Poisson's ratio with different ZrO_2 contents at a residual porosity of 10%

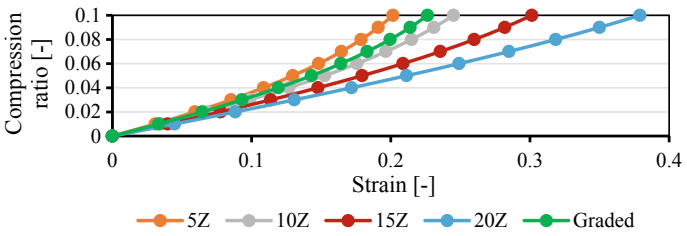

Fig. 8.10 Compression ratio as a function of strain over the Poisson's ratio determined at different ZrO_2 contents

Figure 8.10 shows the dependence of the compression ratio as a function of strain over the Poisson's ratio determined at different ZrO_2 contents, which was previous described for iron powder in the literature [33, 34].

In a composite, this relationship can be described using the following equation:

$$\phi_\rho = \left(25Z^2 - 13.95Z + b\right) \cdot \varphi^2 + 0.2\varphi \tag{8.3}$$

where φ is the strain and b is a material constant of the reinforcement content. In this case, b is approximated to a value of 1.9. This equation was derived from the empirical data to calculate the compression ratio of a composite with a corresponding strain. For this reason, the volume content of the reinforcement phase and the strain are also included in the equation. This equation has a determination coefficient of 0.98 with the empirically determined data.

A comparison of the data with those found in the literature shows that the values for iron powder are slightly higher than those for the TRIP-matrix composite, whereas the values for aluminum MMCs are clearly higher than those for the TRIP-matrix composite. However, note that the reinforcement phase in aluminum MMC is significantly higher at 70% [21]. The same trend (i.e., the values are higher than those for the TRIP-matrix composite) applies to magnesium MMCs that have a reinforcement phase of SiC, wherein the proportion of the reinforcement phase is approximately 30% [35]. Thus, it can be stated that the iron powder comes closest to the values of the TRIP-matrix composite.

8.3.4 Relationship Between Young's Modulus and Density

To determine the axial component of the Young's modulus, the formula of Pavlov et al. [27] was used, which makes it possible to determine the modulus of elasticity through compression tests, which were carried out on a Bähr MDS 830 testing system.

Figure 8.11 clearly shows that the modulus of elasticity increases with increasing ZrO_2 content. Moreover, the modulus of elasticity decreases with increasing residual porosity. This finding is particularly evident at ZrO_2 contents of 15 and 20%. Although the values are almost identical for ZrO_2 contents of 0 and 5%, an increase in the modulus of elasticity can already be seen in the specimen with 10%. The results also clearly show that the specimens with a graded layer structure have a modulus of elasticity between the elastic moduli of the specimens with 10 and 15% ZrO_2. In addition, it can be clearly seen that the measured values of the modulus of elasticity are the same as the values calculated according to the Tsai–Halpin mixing rule [36].

In this composite, the modulus of elasticity can be described using the following equation:

$$E = 90Z + 170\rho_0 \tag{8.4}$$

For simplification, an equation has been derived from the empirical data that agrees with the mixing rule according to Tsai–Halpin. The reinforcing phase and the relative density are included. Here, the relative density plays a larger role than the second phase. This equation has a determination coefficient of 0.95.

Figure 8.12 shows the relationship between the elastic modulus and density. This figure clearly shows that the modulus of elasticity decreases with increasing temperature. Furthermore, the modulus of elasticity increases with increasing density, as described in the literature [37, 38].

The decrease in the modulus of elasticity at elevated temperatures can be described by the temperature dependence of the bonding conditions. Due to the decreasing bonding forces in the matrix, the material flows more quickly. This explains the drop in the modulus of elasticity at elevated temperatures [38]. This change can be described by the following equation:

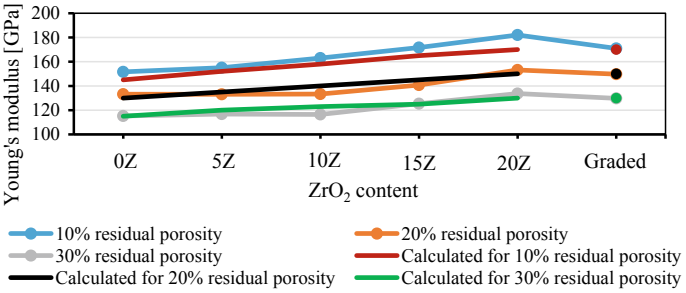

Fig. 8.11 Change in the modulus of elasticity with different residual porosities

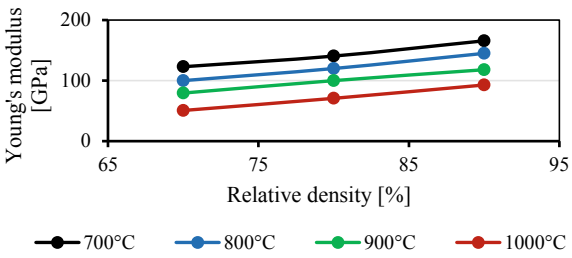

Fig. 8.12 Dependence of the modulus of elasticity on the density of the material with 5Z

$$E = 214\rho_0 - 0.0002T^2 - 0.1T \tag{8.5}$$

This equation was derived from the empirical data for calculating the Young's modulus of a composite at a certain temperature and relative density. For this reason, the density of the specimen and the temperature are also included in the equation. Moreover, the relative density plays a more decisive role in the equation than the temperature. This equation has a determination coefficient of 0.99 with the experimentally determined data.

8.3.5 Oxidation Behavior

For the experimental determination of the scale layer and the associated oxidized specimens were annealed at 1000 °C for 1 h in an inert gas atmosphere and subsequently oxidized in air at intervals of 0, 10, 30 and 60 s. These time periods reflect the transfer times from the furnace to the die in the industry. The oxidation states were then frozen and microsections were made. In addition, calculations of the scale thickness were carried out. This approach was done to simulate the process in industry, where powder forging is usually carried out directly from the sintering furnace. The tests were carried out on compact specimens and porous specimens with a relative density of 80%.

The compact material in Fig. 8.13 shows an average oxide layer of approximately 22 µm. In addition, the scale thickness calculations clearly show that there is a slight difference in the scale thickness of the specimens with 0 and 5% ZrO_2 and that of the specimens with 10 and 20% ZrO_2. In addition, the results show that there is no difference between the sampling times of 0 and 10 s. The first difference observed in the scale thickness of the specimens occurred at a sampling time of 30 s. Here, it can be seen that the specimens with a high ZrO_2 content have a thicker scale than the specimens with a smaller ZrO_2 content. This phenomenon becomes clearer with a sampling time of 60 s.

The porous material in Fig. 8.14 shows an average oxide layer of approximately 66 µm. In addition, the calculations of scale thickness show that there are clear differences between the specimens with 0% ZrO_2, the specimens with ZrO_2 contents of 5, 10, 20% and the graded structure because the latter are already higher than the

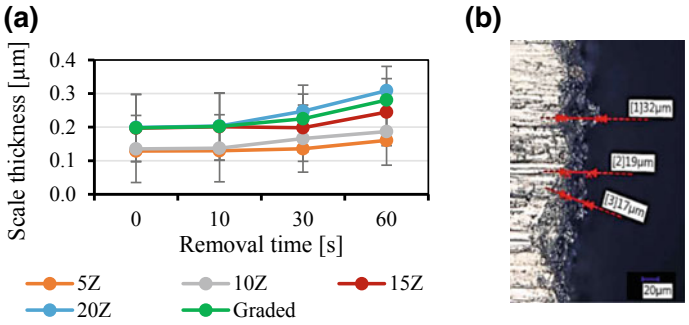

Fig. 8.13 Oxidation behavior of compact material: **a** scale thickness and **b** micrograph

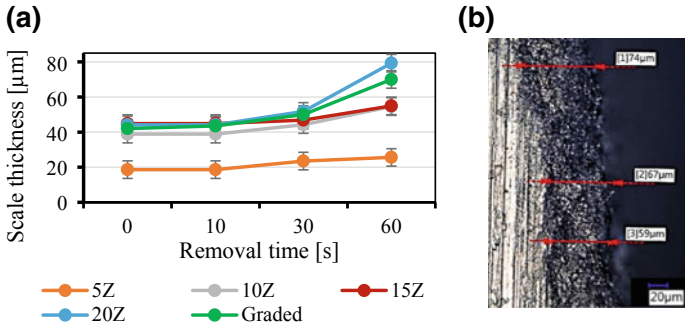

Fig. 8.14 Oxidation behavior of porous material: **a** scale thickness and **b** micrograph

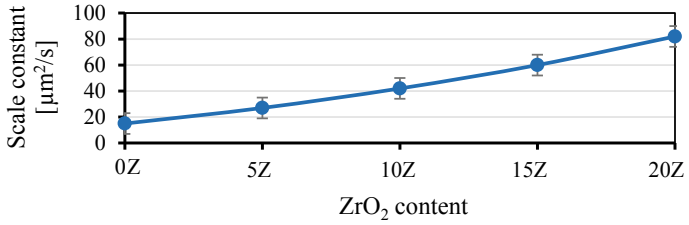

Fig. 8.15 Scale constant as a function of ZrO_2 content at 1000 °C

pure steel at the beginning of oxidation. In addition, there is no difference in specimen oxidation between the removal times of 0 and 10 s; the first notable difference occurred at a sampling time of 30 s. This phenomenon becomes clearer at a sampling time of 60 s. Here, it can be clearly seen that the specimens with ZrO_2 have a larger scale thickness than the specimens without ZrO_2.

This finding means that the different ZrO_2 contents have different scale constants (K_m), as shown in Fig. 8.15; these constants were calculated with the Wagnerian

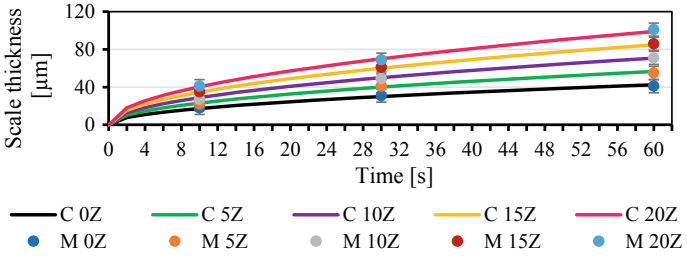

Fig. 8.16 Measured scale thickness at 1000 °C with different ZrO_2 contents (C—calculated and M—measured data)

Fig. 8.17 Temperature dependence of the scale constants

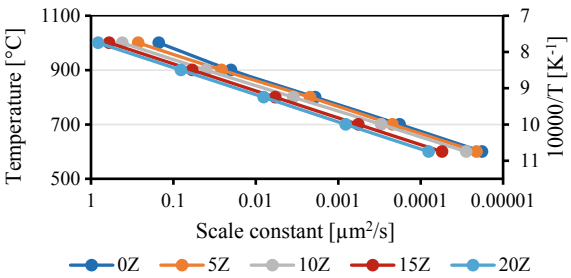

scale theory (parabolic scale growth). The scale constant shown here corresponds to that in the literature [39, 40]. This figure clearly shows that the scale constant increases with increasing ZrO_2 content.

With this scale constant, it is possible to calculate the scale thickness of the individual ZrO_2 contents, as shown in Fig. 8.16. This figure clearly show that with increasing time, the scale layer increases significantly, as reported in the literature [40]. Moreover, with increasing ZrO_2 content, the scale thickness increases. In addition, the simulated values correspond to the measured scale thicknesses.

The results also show that the scale constant is temperature dependent, as previously described in the literature [39, 40]. Figure 8.17 shows that the scale constant behaves linearly at all ZrO_2 contents. In addition, as the ZrO_2 content increases, the curve of the scale constant moves farther away from that of the TRIP steel without ZrO_2.

The oxidation behavior of the specimens generally shows that the scale thickness increases with increasing ZrO_2 content; this phenomenon occurs because the closed surface structure is broken up by the ZrO_2 particles on the surface. This broken structure has more points of attack for oxidation than a closed body. However, note that the porosity of each specimen on the surface is the same as that in the core. The same applies to the values of the porous specimens. Compared to a closed surface, this irregular, porous surface provides a larger area of attack for oxidation. In addition, there is a time factor. Because the porosity increases the area of attack, the more

time there is to oxidize the porous surface, the higher the scale thickness, as shown in Fig. 8.15.

For the same reason, each ZrO_2 content has its own scale constant, which increases with increasing ZrO_2 content in the specimen. The different scale thicknesses can easily be explained by the different scale constants and the different temperature dependencies.

It should therefore be noted that the optimum time for introducing the semifinished products from the sintering furnace into the forging tool is up to 10 s. As previously mentioned, there are no significant deviations in oxidation from a removal time of 0 s in either the nonporous or porous material. Due to the rapid and large formation of oxide layers, it is not advisable to allow for insertion times longer than 10 s.

8.3.6 Process Map Extension for Compressible and Graded Materials

Prasad et al. [41] developed a process map that is helpful in characterizing formability, optimizing the hot forming process and controlling the microstructure of the materials. The only disadvantage is that this process can only be used for incompressible materials. For this reason, this procedure is not applicable to compressible materials such as those used in powder metallurgy. However, in order to create process maps for powder metallurgical production processes that assume a porous initial state, important adjustments must be made. However, powder metallurgical materials can be produced as both homogeneous materials and graded materials. Hence, some adjustments must be made to the compressible material model for the creation of process maps. These modifications include adjustments of the friction due to the different material compositions between the specimen foot and the specimen head and adjustments to the specimen diameter due to the different bulges in the individual layers, which result from differences in composition, stresses, and residual porosity in the individual layers.

Powder forging was simulated on specimens with different ZrO_2 contents and different residual porosities. Therefore, the temperature range 700–1050 °C was investigated. The following conclusions can be drawn from Fig. 8.18.

For TRIP steel, it can be observed that the energy dissipation, starting from a residual porosity of 30% up to a residual porosity of 10%, creates new isolines and strongly shifts the existing isolines. Moreover, the solid material contains considerably fewer isolines than the specimens with residual porosity. In addition, the power dissipation of the compact material is significantly higher (between 15 and 40%) than the power dissipation in the specimens with residual porosity (between 5 and 20%). Furthermore, the only range that does not permit forming is between the forming speeds of 10 and 1 s^{-1} at all temperatures. In addition, component failure occurs at forming speeds of 10^{-1} s^{-1} and 0.1–0.01 s^{-1} in a temperature range of 750–800 and

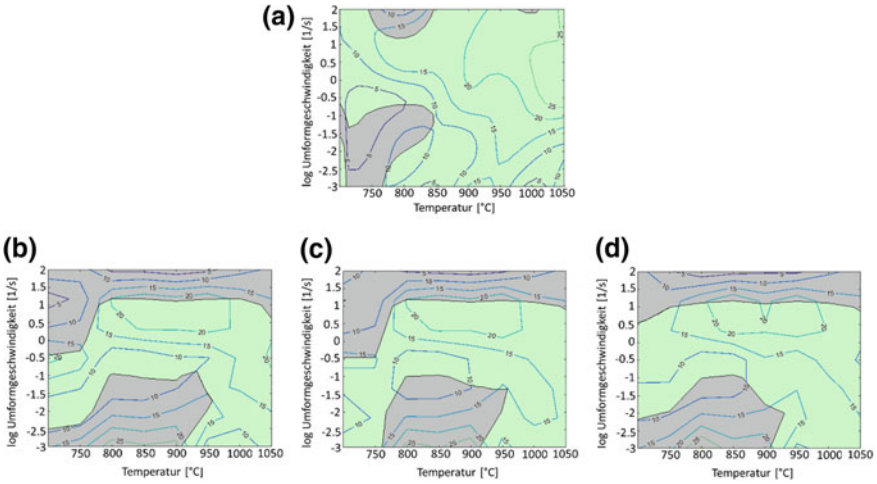

Fig. 8.18 Process maps with 10 vol% ZrO_2: **a** a solid specimen and specimens with residual porosities of **b** 10%, **c** 20% and **d** 30%

900–950 °C. In addition, as the residual porosity increases, the proportion of area where deformation can occur without failure increases.

The unstable area in the upper left corner of all process maps is due to the forming speed. At high forming speeds, the material has no time to absorb the resulting high stresses and subsequently flow. This phenomenon leads to cracking under further external loads. At higher temperatures, the yield strength of the material decreases to such an extent that, despite the rapid deformation, there is greater material flow.

The differences in power dissipation can be explained by the compaction process. Instead of converting energy of the forming process into another form, such as heat, the energy is used to compact the specimen. Therefore, the power dissipation also increases with decreasing residual porosity until reaching a maximum value in the solid material. Detailed and further information can be found in the literature [42].

8.4 Model Experiments on Powder Forging

For the simulation of powder forging and for the verification of the previously obtained data, model experiments of powder forging are presented. Powder forging using the visioplastic method was carried out to investigate the dependence of the shear strain percentage on the compression ratio and the associated mechanical properties. To check the theoretical pore closing behavior during powder forging, metallographic images were examined in various forming stages. In addition, this method was used to investigate the phase angle and boundary between ceramic and steel in order to determine whether the reinforcing particles are firmly embedded

in the matrix and contribute to the mechanical strength. In addition, the relationship between strain and temperature was analyzed to determine the minimum strain required for complete compaction and the temperatures at which optimum and rapid compaction occurs. At the end of powder forging, relative densities of 99.9% were achieved.

8.4.1 Visioplastic Method

The visioplastic method was used to determine the material flow and the associated compaction. For this purpose, cylindrical specimens with a diameter of 10 mm were separated along the sagittal plane and a grid was applied to the inside with a laser (Lasonall XS25, Östling, Solingen, Germany), as shown in Fig. 8.19. The grid mesh was 1 mm, and the depth of the grid was 0.1 mm.

The specimens were recombined. The specimens were compacted in a Gleeble HDS-V40 (Dynamic Systems Inc., Weissenhorn, Germany) (path-controlled) rolling simulator at appropriate temperatures and pressure and in dies 1–3. The temperature was set to 1000 °C, and the strain rate was set to 1 s^{-1}. After forming, the specimen halves were separated from each other again and the grid distortion was measured. Subsequently, with the help of the AutoGrid system (Vialux, Chemnitz, Germany), the major and minor strains were determined.

When considering the residual porosity as a variable parameter, the results show that the strain decreases with increasing residual porosity, as shown in Fig. 8.20. However, the deformed area increases with increasing residual porosity.

This finding can be explained by the increasing compression of the compressible material with increasing residual porosity: with higher residual porosity, there is more volume in the specimen that must first be compacted. This phenomenon leads to very early deformation and to distortion of the applied grid. In contrast, with a low residual porosity (i.e., a small pore volume), the deformation of the component only occurs later because the component exerts a counterforce against the deformation; thus, lower degrees of deformation occur in the samples with low residual porosity. This assertion is confirmed by considering the effective strain. Here, the results show that with increasing residual porosity, the degree of effective strain decreases slightly, whereas the deformed area exhibits a relatively strong increase. This behavior is also

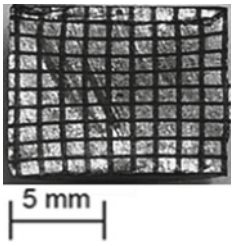

Fig. 8.19 Half of a specimen used for visioplastic analysis after grid preparation

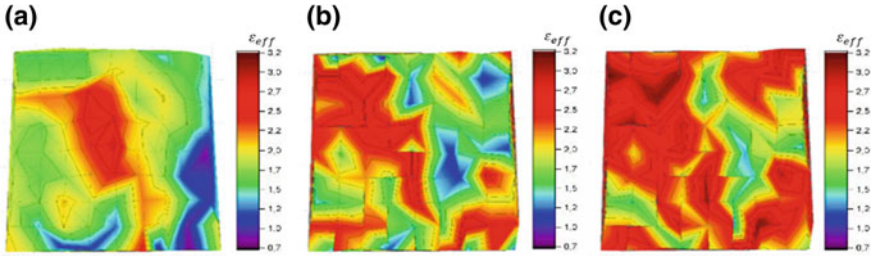

Fig. 8.20 Comparison of effective strain with different residual porosities: **a** 10% residual porosity, **b** 20% residual porosity, and **c** 30% residual porosity

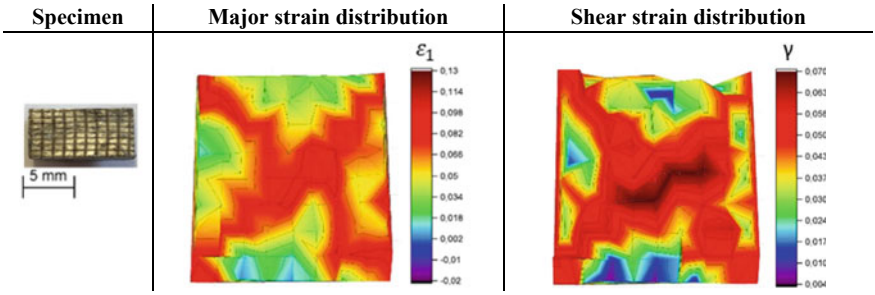

Fig. 8.21 Major strain and shear strain for the specimens in die 1

attributed to the compression of the residual pore volumes in the specimens with increasing residual porosity.

If the different dies (dies 1–3) with their different arrangements of compensating gaps are regarded as variable parameters, then the following information can be determined:

The results show that the major strain is found mainly at the outer corners and in the center of the specimen, as shown in Fig. 8.21. In addition, the specimen shear strain in die 1 is lower than that in the dies, and this shear strain only occurs at the outer corners and in the center of the specimen.

This result reflects the general representation of a forging cross. The creation of the forging cross can be explained simply by Schmid's shear stress law. This phenomenon occurs because the greatest shear stress in a body is at a 45° angle to the main stress axis. For this reason, the largest plastic deformation in the matrix occurs at a 45° angle from the corners of the specimen, which results in a forging cross in a real specimen. Because there are no compensating gaps in die 1 and the material is only compressed and compacted, a significant shearing of the component occurs. The typical bulging of the specimen during the formation of the forging cross is prevented by the die. The very slight shear strain is due to compression and the associated material flow during compression.

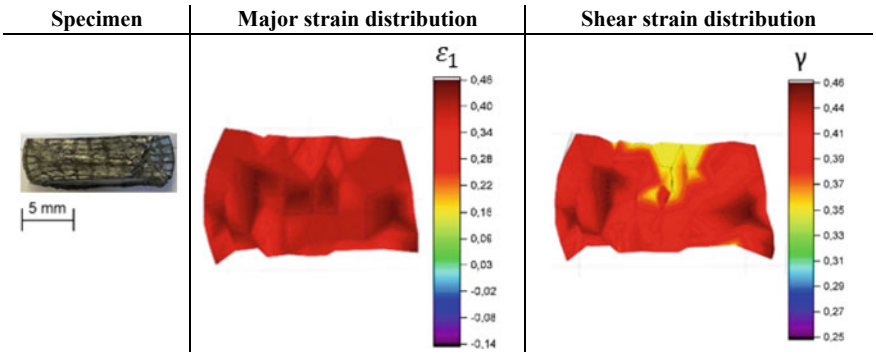

Fig. 8.22 Major strain and shear strain for the specimens in die 2

With die 2, the major strain is highest and can be found nearly exclusively at the level of the compensating gap. The material that has not flowed into the compensating gap shows nearly no deformation compared to the rest of the specimen, as shown in Fig. 8.22. A shear strain analysis shows that the specimen shear strain in die 2 is higher than that in the other two dies. Moreover, the highest shear strain is found in the area of a compensating gap, whereas there is approximately no shear strain in the area without a compensating gap.

This finding must be explained in terms of the material flow into the compensating gap during forming. When the material flows into the compensating gap, the specimen is subjected to a large shear, which results in a large deformation of the specimen and a very high major strain distribution. This phenomenon is verified by the proportion of shear strain in the specimen, which can also only be found in the area of the compensating gap. Due to this shear and the material flow, a forging cross is not formed. However, a high shear strain rate results in a strong compression of the specimen, as is the case in theory.

The specimen strain in die 3 is between that in dies 1 and 2. In addition, the largest major strain can also be seen at the outer edges and in the center of the specimen. With this die, the proportion of shear strain is concentrated primarily on the center and on the tips of the outer edges, whereas in other areas, there is approximately no shear strain, as shown in Fig. 8.23. Detailed and further information can be found in the literature [43].

On the one hand, this behavior can be traced back to the forging cross, which forms in the center of a body during compression. The high shear rates at the outer corners of the specimens are due to the shear of the specimen material with the punch, as the material flowed into the compensating gap at the desired points. However, note that the shear strain experienced by the material in this way is substantially lower than the shear strain produced by the structure of die 2. Thus, the density of the test specimens from die 3 is also lower than that of the test specimens from die 2.

If the relative density is now compared with respect to the selected die and the ZrO_2 content, it can be seen that the highest relative density was achieved with the dies

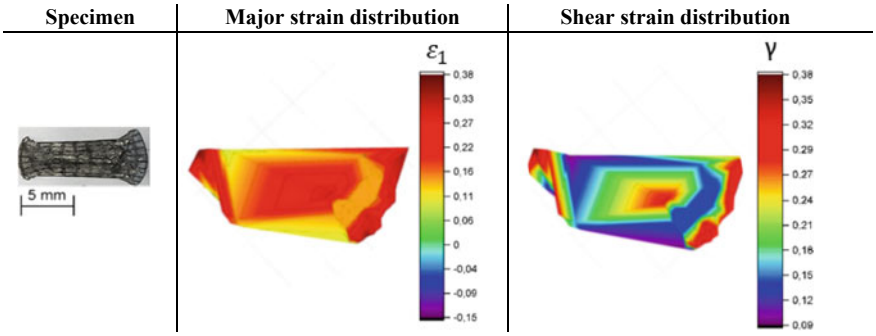

Fig. 8.23 Major strain and shear strain for the specimens in die 3

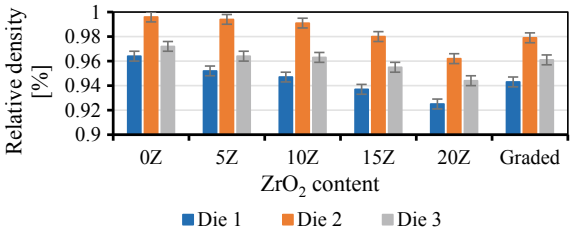

Fig. 8.24 Comparison of relative densities with different dies and ZrO_2 contents

with compensating gaps. In addition, as the ZrO_2 content increases in the specimens, the relative density of the final components decreases, as shown in Fig. 8.24. The change in theoretical density with increased ZrO_2 content was taken into account.

The large difference in the maximum relative densities achieved can be explained by the dies and the associated forming conditions. With pure compression without transverse flow, die 1 represents pure repressing. The state of the art is in agreement that with pure repressing only, relative densities up to a maximum of 95–96% are possible [1, 12, 44, 45, 46, 47, 48]. Therefore, the values measured here are in a very high range with respect to the achieved densities. Dies 2 and 3 have compensating gaps and should achieve a relative density of 100% due to the transverse flow of the material. This relative density was nearly achieved in some of the specimens in die 2. However, for die 3, the relative density of 100% was not reached due to the high stress on the matrix in the shear zone. Due to this stress, new pores and cracks occur within the specimen, as shown in Fig. 8.25. For this reason, complete compaction of the material is not possible in die 3.

The decreasing final density of the specimens with increasing ZrO_2 content is due to the increasing hydrostatic stresses in the matrix of the material, which increase due to the increasing number of reinforcing particles. These hydrostatic stresses oppose the yield stress, thereby inhibiting the material flow. However, shear strain and the associated material flow are the main mechanisms for the compression of compressible bodies. Thus, a compression of the specimens with a high ZrO_2 content is not exactly given, as with specimens with a low ZrO_2 content.

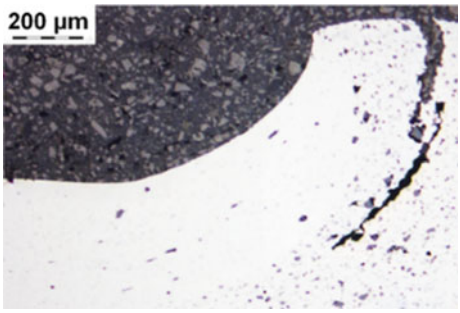

Fig. 8.25 New pores and cracks that appear during forming in die 3

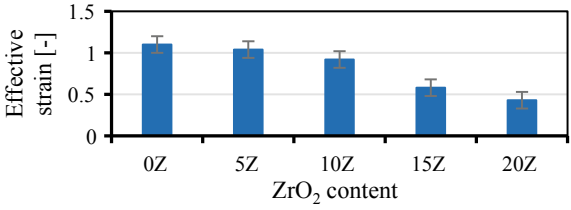

Fig. 8.26 Effective strain at different ZrO_2 contents in die 2

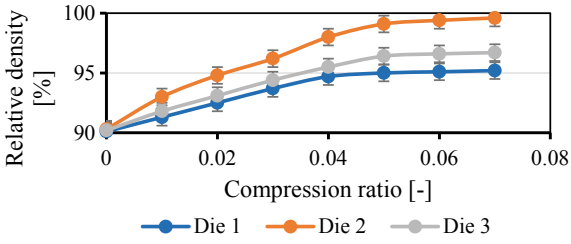

Fig. 8.27 Relationship between compression ratio and relative density for a specimen with a residual porosity of 10% and 5Z

An examination of the effective strain with variable ZrO_2 contents from die 2 shows that with increasing ZrO_2 content, the effective strain decreases strongly, as shown in Fig. 8.26. In addition, the deformed surface remains nearly constant.

These findings lead to the conclusion that as the ZrO_2 content increases in the samples, the hydrostatic stresses in the sample volumes increase due to the particle reinforcement and thus a material flow is inhibited. Thus, the force required for the same degree of deformation is increased accordingly. Hence, the particle amplification represents an obstacle for the material flow and generates a hydrostatic stress field that counteracts the stress field of the flowing material and brings a portion of the material to a standstill, which makes a postcompaction of the compressible material into the compact state more difficult or impossible.

Note that the presence of compensating gaps and a high effective strain lead to a high relative density and that the arrangement of the compensating gaps plays an essential role in the compaction, as shown in Fig. 8.27. The results clearly show

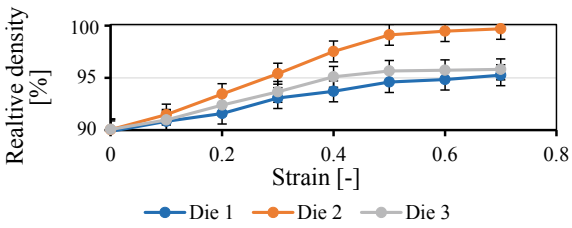

Fig. 8.28 Influence of the strain on the density during powder forging with the different dies at a working temperature of 1000 °C and 5Z

that dies 2 and 3 achieve a higher relative density than die 1 at the same degree of compression.

Thus, the arrangement of the compensating gaps plays a decisive role. The arrangement of the compensating gap must ensure that the greatest possible shear strain is generated in the component and that the greatest possible material flow is achieved. This influence of the compensating gap arrangement is demonstrated by the fact that the compaction in die 2 is greater than that in die 3, although both have compensating gaps.

The relationship between strain and temperature is investigated to find the minimum strain required for complete compaction and at which temperatures optimum and rapid compaction occurs.

To find the die with the best compression properties, the individual relative densities of the specimens were compared with the matrices depending on the strain. Figure 8.28 shows the influence of the strain on the relative density in labor tests with the different dies.

In addition, the results show that from a strain of 0.5, no significant compaction of the specimen occurs. Overall, the maximum achievable density is highest for die 2 at 99.8%, followed by die 3 at 96.3%, and finally by die 1 at 94.6%; note that die 1 was designed without a compensating gap and represents a pure postcompaction. The case of die 1 represents the worst compaction to solid material. From this finding, it can be deduced that the matrices with compensating gaps have a higher density than the matrices without compensating gaps. Thus, a higher density is achieved if transverse flow or shear strain occurs in the material.

The increase in density in die 3 is weaker than that in die 2, which is due to the arrangement of the compensating gap and the associated different shear deformation. In die 2, the material shears the specimen by a transverse extrusion process, whereas in die 3, there is a pure upsetting first and then shearing at the punch edges. According to the state of the art, the decisive factor for compaction is the hydrostatic stress component; however, for optimum full compaction, a certain mixture of hydrostatic stress component and shear strain is more suitable. Based on the available data, it can be assumed that the shear strain must correspond to the hydrostatic stress to achieve full compaction and that the shear strain should not begin subsequently as with die 2. Therefore, the arrangement of the compensating gaps in the die plays a decisive role in compaction.

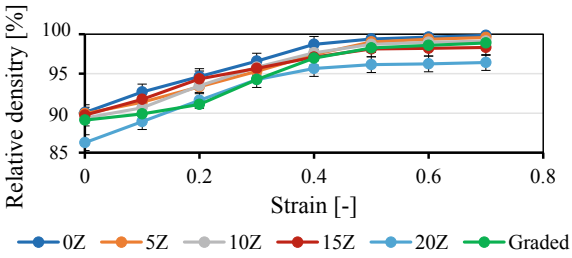

Fig. 8.29 Influence of the strain on the density in die 2

Figure 8.29 shows the influence of the different ZrO_2 contents and the strain on the density during powder forging with die 2. Note that the possible compaction decreases with increasing ZrO_2 contents. However, a higher density can be achieved overall with die 2 (i.e., with compensating gaps) than with die 1. In addition, from a strain of 0.5, no significant compaction of the specimen takes place. The increase in density from a strain of 0.5 is greater in die 2 than in die 1. In the case of specimens with a ZrO_2 content of 15 and 20%, the compaction is even less. Additionally, this phenomenon can be traced back to some measuring tolerances in the determination of the density. A maximum density of 99.8% can be achieved with a ZrO_2 content of 5%.

The differences in compaction between the individual ZrO_2 contents are due to particle reinforcement. With increasing ZrO_2 content in the specimens, the initial density of the specimens decreases. As previously stated, the stress field emanating from the reinforcing particles works against the hydrostatic stress component required for compaction. Since the ZrO_2 cluster formation additionally reinforces the stress fields, the material flow and the subsequent compaction nearly comes to a standstill. The reason that a higher compaction is still possible with these high ZrO_2 contents in die 2 lies in the previously described compensating gaps and the breakage of particle clusters due to shear strain. These phenomena allow material flow and compaction. However, from a ZrO_2 content of 20%, the stress field of the particles seems to be so large that even the shear strain is not sufficient to overcome it.

Furthermore, the specimens do not undergo significant compaction after a strain of 0.5. This finding could be explained by the fact that the material has already undergone full shear deformation in the compensating gaps; thus, a sharp increase in density has already occurred. Therefore, the specimen is now compressed and compacted only by postcompaction and no longer by shear strain. This compression only has a slow increase in relative density, which explains the slow increase in density from a strain of 0.5. Detailed an further information can be found in the literature [49].

8.4.2 Metallographic Examination

To examine the microstructure, metallographic microsections were carried out at each strain and the microstructure was analyzed. The images were taken at the forging cross of the specimens from die 2, as shown in Fig. 8.30. In this case, the specimen contains only 5Z. The residues on the specimens originate from V2A etching.

The metallographic examination (Fig. 8.31) shows the microstructure and some artifacts of the V2A etching, which are marked here as gray areas. Moreover, it is clearly visible that at a strain of 0, the individual grains of the TRIP matrix and the reinforcing particles are still visible. With increasing strain, the holes are compressed and stretched, as described in the literature [27, 50], until a large pore becomes many finely distributed pores. These pores are compressed and distributed by the beginning material flow, as observed in the microstructure of the specimen with a strain of 0.3. Moreover, the microstructure of the specimen with a strain of 0.3 is finer than the individual powder particles in the microstructure with a strain of 0. This phenomenon becomes very clear at a strain of 0.5. The results show that the material recrystallizes during powder forging. However, this recrystallization process is not accelerated or excited by the reinforcing particles since these particles are above a particle volume fraction-to-particle size ratio of 0.2 μm^{-1}; therefore, according to some authors, the particles do not support recrystallization [35, 51]. The grain size at the beginning of powder forging, measured via laser granulometry, was 37 μm, whereas the grain size after powder forging was only 19 μm, which confirms recrystallization.

For the analysis of the surfaces of the individual layers of the graded layer structure after forming, metallographic images of the surfaces of the individual phases were made according to different strains. These images were taken because these areas

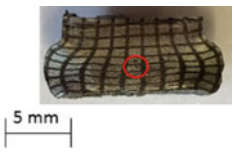

Fig. 8.30 Illustration where the microstructure of the specimens from die 2 were recorded

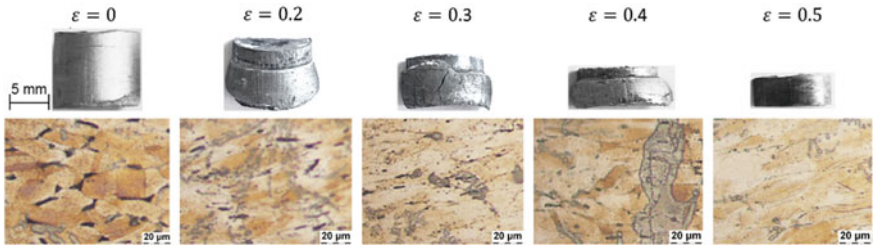

Fig. 8.31 Microstructure at the corresponding strain at the center of the specimen

that are most susceptible to interference (i.e., weak spots) in graded layer structures. These locations are particularly susceptible to interference due to the different stress fields in the individual layers. To fully utilize the mechanical properties of these components, a good connection of the individual phases is very important.

At the interface of the individual layers of the graded layer structure, no special features in the sense of defects can be recognized; however, the different ZrO_2 content is clearly recognizable, which distinguishes the layers from each other. Figure 8.32 also shows the bulging structure in the graded specimen at a strain of 0.4. This bulging structure deviates from the symmetric barrel-shaped bulge of homogeneous specimens. This deviation was taken into account when calculating the process maps of compressible graded materials; this phenomenon was mathematically described in that section.

8.4.3 Formation of the Interfaces of Phases

For the analysis of the ceramic/steel interfaces, metallographic images were taken both in the shear zone (Fig. 8.33) and in the forging cross (Fig. 8.34) of a specimen from die 2 after powder forging at 1000 °C.

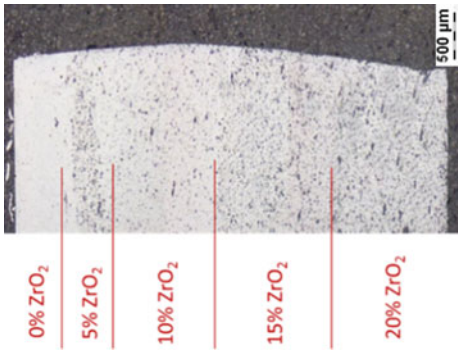

Fig. 8.32 Micrograph through the different layers of a graded specimen

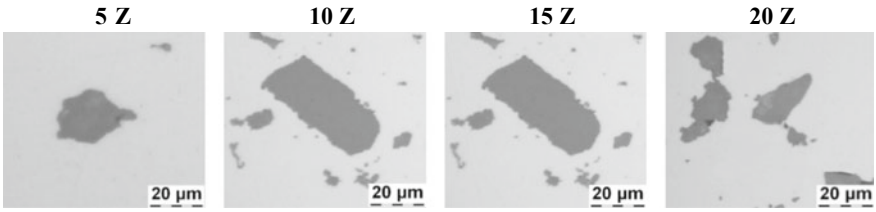

Fig. 8.33 Ceramic/steel interface in the shear zone with corresponding ZrO_2 contents

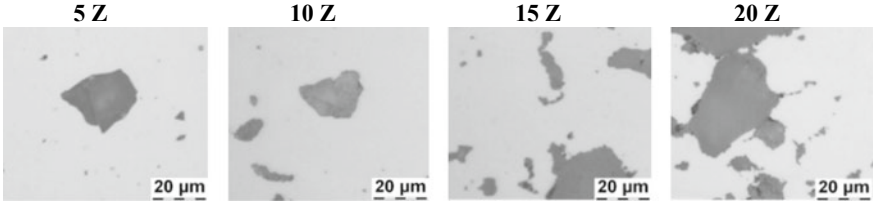

Fig. 8.34 Ceramic/steel interface in the forging cross with corresponding ZrO_2 contents

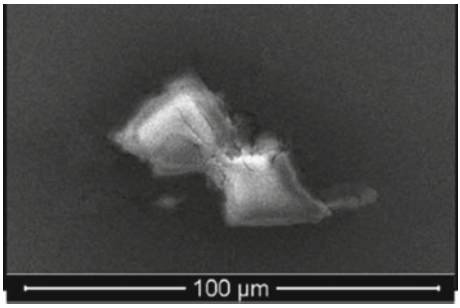

Fig. 8.35 SEM image of the interphase ceramic/steel at a ZrO_2 content of 10% (HV: 20 kV; WD: 10; and Mag.: 2000)

The microstructures in the shear zone of the specimens show a fixed bond between the reinforcing particle and the matrix for the specimens with 5, 10 and 15% ZrO_2. In addition, no pores or cracks are visible. In the specimen with 20% ZrO_2, pores or holes in the steel matrix are visible at the poles of the particles. Thus, there is no 100% binding of the reinforcing particles to the matrix. Smaller and isolated particles are fully bound to the matrix, whereas large particles or whole particle clusters show corresponding pores in the matrix.

The images in the forging cross of the specimens show that the specimens with ZrO_2 contents of 5, 10 and 15% also exhibit a firm bond between the reinforcing particle and the matrix. The specimen with 20% ZrO_2 also shows pores in the matrix and in the shear zone. However, the pores are more frequently found in the matrix than in the shear zone.

Images from a light microscope indicate that the specimens with a low particle content show a good phase bonding between matrix and reinforcing particles. This good phase bond is also visible during scanning electron microscopy (SEM) observations, as shown in Fig. 8.35. This finding confirms the assumptions from the light microscope images.

However, fewer pores are present in the specimens in the shear zone than in the specimens in the forging cross. This discrepancy can be explained by the hydrostatic stress field and the yield stress. As the ZrO_2 content increases, stresses form in the matrix that counteract the hydrostatic stress, thereby preventing the specimen from compacting. These yield stresses become particularly large in clusters of reinforcing particles. These stresses can become so great that they completely stop the flow of material. The difference in the residual porosity between the shear zone and

the forging cross is mainly to be found in the forming or the material flow. Since the specimens in the shear zone undergo a large deformation due to the shear and the associated shear strain, there is a greater yield stress in this section, as shown in Sect. 8.4.1; thus, a greater material flow occurs due to the compression of the specimen. In the case of the specimens in the forging cross, no correspondingly high shear strain occurs due to the lack of a strong material flow, which can also be seen from the only slightly distorted grid on the specimen in Fig. 8.21. As a result, the yield stress is sufficiently large to counteract the hydrostatic stress field and to subsequently counteract full compaction. This assertion is supported by the increased occurrence of pores in places where many particles meet. Detailed and further information can be found in the literature [52].

8.4.4 Mechanical Properties

When considering the hardness distribution within the different dies, as shown in Fig. 8.36, the highest density is achieved in die 2, whereas die 1 produces the lowest hardness.

These results can be explained by the density of the specimens. The higher the density of the specimen is, the better the mechanical properties and the higher the hardness of a powder-forged specimen. The highest compaction was achieved in die 2. The hardness measurements showed that the hardness of the specimens increased with increasing ZrO_2 content. This increase in hardness can be explained by the fact that the reinforcing particles counteract the deformation caused by the hardness tester.

It is possible to calculate the tensile strength of a material from the hardness of the material [53]. According to this model, the data from Fig. 8.37 were collected.

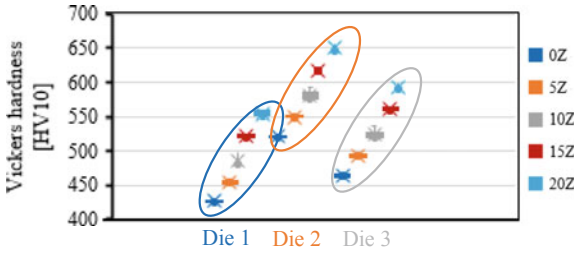

Fig. 8.36 Hardness distribution at different ZrO_2 contents in the different dies

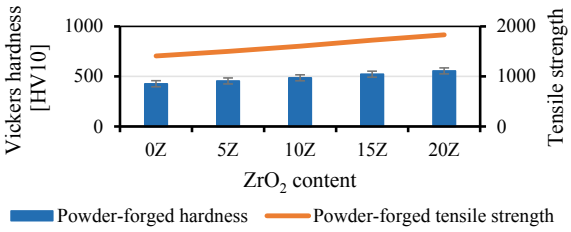

Fig. 8.37 Hardness and tensile strength after powder forging in die 2

8.4.5 *Shear Strength of the Layers with a Graded Layer Structure*

The adhesion of the layers of the graded layer structure was measured in the graded material systems to determine the shear strength of the individual layers and to be able to make possible predictions for the failure location. When measuring the shear strength of the individual layers, it was found that with increasing ZrO_2 content in the individual layers, the shear strength generally decreases, as shown in Fig. 8.38.

With increasing ZrO_2 content, the shear strength decreases on average by 17% with increasing ZrO_2 content, both in forged and sintered specimens. In addition, the shear strength of forged specimens is significantly higher than that of sintered specimens. On average, the shear strength of forged specimens is 72% higher than that of sintered specimens.

This phenomenon can be explained by the increase in reinforcing particle fractions and the fact that as the number of particles contained in the matrix increases, the amount of matrix present at the interface of two layers decreases. Similarly, the poles represent flaws where crack initiation begins. These flaws also increased with increasing ZrO_2 content.

When comparing the shear strength of the individual layers with data from similar cladding processes used to coat materials onto a steel sheet, the values of the layers of the graded layer structure appear to be on the same level or higher than the values in the literature, as shown in Fig. 8.39. Only the stainless steel cladded on a steel sheet achieved an adhesive strength of 200 MPa [54–56].

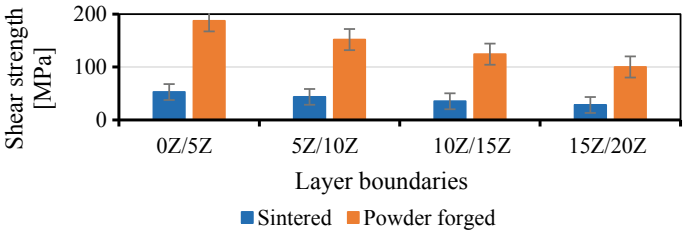

Fig. 8.38 Adhesion of individual layers before and after powder forging

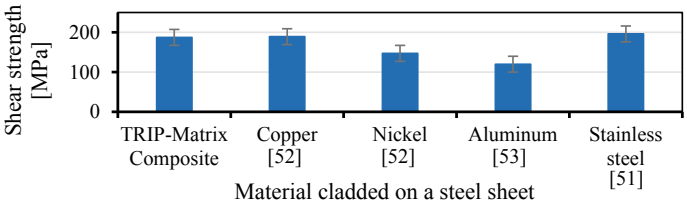

Fig. 8.39 Shear strength of materials cladded on a steel sheet

The shear strength in relation to the compaction ratio, as shown in Fig. 8.40, indicates that the shear strength of the layers increases with increasing compaction ratio. In addition, increasing the compaction ratio increases the shear strength of the forged specimens more than that of the sintered specimens. This phenomenon can be described by the following equation:

$$S = \Phi_{\rho}(c \cdot \rho_0) \tag{8.6}$$

where c is a material constant with a value of 2013 and ρ_0 is the relative density. Due to the differences in density between powder-forged and sintered specimens, the relative density of the specimen plays a decisive role in the equation, as does the compression ratio. This equation has a determination coefficient of 0.98 with the experimentally determined data.

These results can be explained by the compression itself. In the case of the specimens prior to powder forging, only sintered necks hold the specimen together, whereas the powder-forged specimens have a microstructure. The force required to break a sintered neck is much less than the force required to introduce sufficient energy into the matrix to maintain crack initiation and propagation.

Fig. 8.40 Comparison of adhesive strength and compaction degree

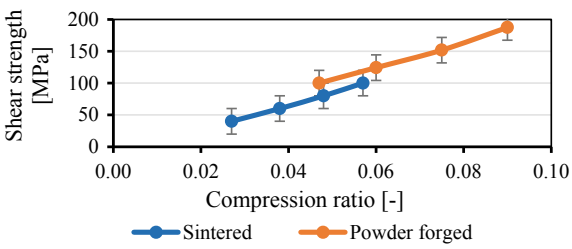

8.5 Conclusions

In general, this study showed that ZrO_2 particle-reinforced TRIP steels can be produced via the powder metallurgical route and that the produced samples achieved solid material densities and exhibited enhanced mechanical properties.

In addition, this same production approach can produce components with graded particle reinforcements and compact the components to a density of solid material without losing the graded structure. The following process parameters were the most successful for the process route. The highest obtained density was achieved in dies with compensating gaps, in which shearg occurred immediately during forming. If the compensating gaps are arranged in such a way that only a pure compression followed by shear occurred, a compact material was not produced; the same phenomenon occurred when no compensating gaps were used. In addition, the highest densities were achieved at a temperature of 1000 °C and a strain of 0.5 in the same die. In addition, up to a reinforcement particle content of 10%, excellent bonding was observed between the reinforcement particles and the matrix.

Acknowledgements This work was funded by the Deutsche Forschungsgemeinschaft (DFG, German Research Foundation), project number 54473466—SFB 799, subproject A6.

References

1. W. König, R.S.G. Röber, Umformtechnikmagazin **426** (1992)
2. G. Röber, Powder forging of gearwheels in layered composite technology—stress-compliant production and component behaviour, Doctorate thesis, RWTH Aachen, 1991
3. K. Vossen, Powder forging of spur and helical cylindrical gears, Doctorate thesis, RWTH Aachen, 1987
4. M. Abdel-Rahman, M.N. El-Sheikh, J. Mater. Process. Technol. **97** (1995)
5. T. Nakagawa, T. Amano, K. Obara, Y. Nishino, Y. Maeda, in *13th International Machine Tool Design and Research Conference* (1972), p. 455
6. A. Salak, Hutnicke Listy 418 (1990)
7. G. Zapf, *Engineering Handbook. Primeval Forming* (Carl Hanser Verlag, München, 1981)
8. H.A. Kuhn, B. Lynn, Metal Powder Industries (1990)
9. H.E. Exner, H. Danninger, *Gmelin Handbook of Inorganic Chemistry, Metallurgy of Iron. Powder Metallurgy of Steel*, 10th edn. (Springer, Berlin, Heidelberg, 1992)
10. F.J. Esper, *Powder Metallurgy. The Flexible and Advanced Method for Economical and Reliable Components; with 15 Tables* (Expert-Verlag, 1996)
11. G. Durrant, V.D. Scott, Compos. Sci. Technol. **49**, 153 (1993)
12. G. Eberhardt, *Powder Forging. Manufacturing Technology* (Hochschule, Pforzheim, 2013)
13. W. Schaub, M. Stilz, R. Geiger, *Forming technology—Handbook for Industry and Science. Volume 4: Special Processes, Process Simulation, Tool Technology, Production*, 2nd edn. (Springer, Berlin, 1993)
14. P.B. Prangnell, S.J. Barnes, S.M. Roberts, P.J. Withers, Mater. Sci. Eng., A **220**, 41 (1996)
15. B.-A. Behrens, N. Vahed, H. Brand (eds.), *Powder Metallurgical Production of Graded Tool Materials* (Verlag Meisenbach, Bamberg, 2013)
16. F. Klocke, W. König (eds.), *Fertigungsverfahren 5, Gießen, Pulvermetallurgie, Additive Manufacturing*, 4. Auflage (Springer Vieweg, Berlin, Heidelberg, 2015)

17. F. Klocke in *Fertigungsverfahren 5. Gießen, Pulvermetallurgie, Additive Manufacturing*, ed. by F. Klocke, W. König (Springer Vieweg, Berlin, Heidelberg, 2015), p. 39
18. M. Krehl, *Einführung in die Pulvermetallurgie* (FPM, 2019)
19. G. Arth, A. Samoilov, Berg Huettenmaenn Monatsh **157**, 306 (2012)
20. D. Rogowski, Process for the preparation of preforms for metal matrix composites, Patentschrift: DE 10 2008 054 561 A1 (2009)
21. H. Engel, *Sintered Materials from Non-ferrous Metals* (Springer, Berlin, Heidelberg, 1993)
22. I. Lenke, *Metall Matrix Composits* (Thinking Ceramics, CeramTec, Plochingen, 2002)
23. G. Zapf, Mater. Sci. Technol. **171** (1979)
24. R.L. Coble, *Reactive Sintering* (MIT, Cambridge, MA, 1984)
25. V.V. Skorokhod, *Mechanism for Improving the Mechanical Properties of Sintered Iron–Copper Composites Alloyed with Molybdenum*
26. S. Mäkipirtti, On the sintering of W-Ni-Cu heavy metal. Zugl.: Helsinki, Inst. of Technology, Diss., 1959 (The Finnish Acad. of Technical Sciences, Helsinki, 1959)
27. V. Pavlov, M. Nosenko, B. Popov, S. Jakunin, Poroshkovaja metallurgija **20** (1987)
28. TU Graz (ed.), *The Physical Properties of Steels „The 100 Steels Programme"*, Part I: Tables and Figures (Graz) (1994)
29. U. Frank, The Piosson's ratio of plastics, illustrated by the example of amorphous thermoplastics, Dissertation, Universität Stuttgart, 1984
30. H.A. Kuhn, C.L. Downey, Int. J. Powder Metall., **15** (1971)
31. W. Schatt, K.-P. Wieters, B. Kieback, *Powder Metallurgy. Technologies and materials*, 2., bearbeitete und erweiterte Auflage (Springer, Berlin, Heidelberg, 2007)
32. H.A. Kuhn, M.M. Hagerty, H.L. Gaigher, A. Lawley, (New York, Plenum Press, 1971), p. 463
33. N. Nguyen, Influence of process parameters in powder forging on the properties of the finished workpieces, Doctorate thesis, TU Bergakademie, Freiberg, 1995
34. B. Lorenz, A contribution to the theory of forming powder metallurgical initial forms, Habilitation thesis, TU Freiberg, 1995
35. L. Ceschini, G. Minak, A. Morri, F. Tarterini, Mater. Sci. Eng., A **513–514**, 176 (2009)
36. J.C. Halpin, S.W. Tsai, Air Force Materials Laboratory (1967)
37. W. Bleck, S. Münstermann, *Einflußgrößen auf den Elastizitätsmodul von Stählen für den Fahrzeugbau,* Forschungsvereinigung Automobiltechnik, 182 (2004)
38. H. Foell, *Elastische Module*, Material Science 1, Universität Kiel, (2015)
39. D. Hünert, *Corrosion processes and carburization of ferritic-martensitic steels in H2O-CO2 atmospheres*. Doctorate thesis TU Bergakademie Freiberg, 2010 (Bundesanstalt für Materialforschung und -prüfung (BAM), Berlin, 2010)
40. R. Viscorová, Investigation of the heat transfer during splash water cooling under consideration of the influence of scaling, Doctoral thesis, TU Clausthal (2007)
41. Y.V.R.K. Prasad, K.P. Rao, S. Sasidhara, *Hot Working Guide. A Compendium of Processing Maps*, 2nd edn. (ASM International, Materials Park, OH, 2015)
42. M. Kirschner, Mater. Sci. Forum **2019**, 15 (2019)
43. M. Kirschner, R. Eckner, S. Guk, L. Krüger, R. Kawalla, U. Prahl, Deformation behavior of particle reinforced TRIP steel / Mg PSZ composite at hot working temperatures. Steel Res. Int. (2018). https://www.doi.org/10.1002/srin.201800334
44. B.-A. Behrens, T. Yilkiran, N. Vahed, C. Frischkorn (eds.), *Influence of Material Flow on Compaction During Sinter Forging* (2014)
45. F. Li, J. Yi, J. Eckert, Metall. Mat. Trans. A **48**, 6027 (2017)
46. H. ElRakayby, H. Kim, S. Hong, K. Kim, Adv. Powder Technol. **26**, 1314 (2015)
47. G.-S. Shim, M.S. Kim, W.Y. Kim, H. Yamagata, MSF **439**, 40 (2003)
48. A. Salak, M. Selecká, Powder Metall. Prog. **3** (2005)
49. M. Kirschner, S. Guk, Beitrag zur Bewertung des Verdichtungsgrades mittels Visioplatsizität. Kongress & Fachmesse Werkstoffwoche 2019, Dresden, den 18–20.09.2019, Dokumenten-Bibliothek der Deutsche Gesellschaft für Materialkunde e.V. (2019)
50. A. Flodin, M. Andersson, A. Miedzinski, Met. Powder Rep. **72**, 107 (2017)

51. K.K. Deng, X.J. Wang, W.M. Gan, Y.W. Wu, K.B. Nie, K. Wu, M.Y. Zheng, H.G. Brokmeier, Mater. Sci. Eng., A **528**, 1707 (2011)
52. M. Kirschner, S. Guk, R. Kawalla, U. Prahl, Forming complex graded and homogeneous components by joining simple presintered parts of TRIP-matrix composite through powder forging. Metals (2020)
53. R.J. Meyer, E. Pietsch (eds.), *Eisen - Härteprüfverfahren*, Beziehung zwischen Härte und Zugfestigkeit, Achte Völlig neu Bearbeitete Auflage (Springer, Berlin, Heidelberg, s.l., 1974)
54. W. Rädeker, Steel and Iron (1938)
55. H. Schaumburg, *Materials* (Vieweg + Teubner Verlag, Wiesbaden, 1990)
56. M. Schmidtchen, R. Kawalla, in *Rolling of Flat Products*, ed. by H.G. Bauer, W. Schadt (Springer, Berlin, 2017), p. 87